Defence Technology 59 (2026) 149–165

Contents lists available at ScienceDirect

Defence Technology

journal homepage: www.keaipublishing.com/en/journals/defence-technology

Adaptive RF stealth for next-generation long-range cruise missiles through interdisciplinary integration of MnZn ferrite/epoxy RAM and sea-surface multipath null exploitation

Renan Richter [a,*], Ioannis Vagias [b], Thalita Sani-Taiariol [c], Newton A.S. Gomes [a], David Bacci [d], Maurício R. Baldan [c]

[a] Aeronautics Institute of Technology - ITA, Praça Marechal Eduardo Gomes, 50, São José dos Campos, 12228-900, São Paulo, Brazil
[b] Cranfield Defence and Security/Defence Academy of the UK, Shrivenham, SN6 8LA, United Kingdom
[c] National Institute of Space Research - INPE, Av. dos Astronautas, 1758, São José dos Campos, 12227-010, São Paulo, Brazil
[d] Oxford Thermofluids Institute/University of Oxford, Oxford, OX2 0ES, United Kingdom

ARTICLE INFO

Article history:
Received 24 July 2025
Received in revised form
14 October 2025
Accepted 7 November 2025
Available online 10 November 2025

Keywords:
Cruise missiles
Electromagnetic simulation
Radar absorbing material (RAM)
Radar cross section (RCS)
Multipath propagation
Stealth

ABSTRACT

This study presents an interdisciplinary framework to enhance the radar cross-section (RCS) reduction of next-generation long-range cruise missiles by integrating MnZn ferrite/epoxy-based radar-absorbing materials (RAM), electromagnetic simulation, and multipath-aware flight profiles. The best-performing RAM exhibited a reflection loss of −23 dB at 9.8 GHz with a 3.4 GHz effective absorption bandwidth, supported by complex permittivity/permeability analysis and Lorentz-based dispersion modeling. When applied to realistic missile geometries, simulations showed RCS reductions exceeding 25 dB. Furthermore, integrating this material into a dynamic radar detection algorithm shows how sea-surface multipath effects can increase the generation of null channels, reducing reaction time by up to 94 s under simulated conditions. Results underscore the effectiveness of integrating RAM with adaptive trajectory profiles to develop new doctrines for future radio-frequency (RF) low-observable, long-range cruise missiles.

1. Introduction

The introduction of long-range cruise missiles in the 1970s marked a pivotal shift, balancing operator safety from standoff positions with precise strategic strikes to minimize collateral damage. This capability was made possible through advances in missile propulsion, flight mechanics, fire control sensing, and guidance-navigation-control (GNC) systems. These advances extended missile range and improved the weapon's survivability and accuracy. As a result, cruise missiles have gained prominence in recent conflicts for their ability to neutralize high-value targets such as integrated air defense systems, command and control (C^2) nodes, and critical infrastructure. Moreover, they allow human-crewed aircraft to conduct stand-in operations in contested airspace with increased personnel survivability.

However, as cruise missiles have evolved into strategic assets, so have early warning radar systems, employing phased array radars and space-time adaptive processing (STAP) to counter low-altitude subsonic threats. Consequently, future cruise missiles must be stealthier and more agile to deny, delay detection and acquisition, and counter soft-kill and hard-kill effectors. Combining radar-absorbing materials (RAM) with the lobing effects induced by sea-surface multipath propagation in maritime environments is an alternative to deny radar detection.

Previous studies have focused on radio-frequency (RF) low observability (LO), and RAM explored the use of magnetic fillers and polymer matrices to develop effective absorbing and shielding coatings [1–3]. Ferrites and their composites offer several key advantages for air vehicle stealth, including high resonance frequencies, elevated resistivity, low density, chemical stability, vigorous absorption intensity, and broad operational bandwidths [4]. Epoxy resins have been widely studied for their high electrical resistivity, low dielectric constant, corrosion resistance, and ease

* Corresponding author.
E-mail address: richter@ita.br (R. Richter).
Peer review under the responsibility of China Ordnance Society.

https://doi.org/10.1016/j.dt.2025.11.010

of processing and forming [5].

Earlier investigations by Gama [6,7] highlighted variations in complex permeability and permittivity of MnZn ferrite-based RAM at microwave frequencies (2 GHz–18 GHz), emphasizing the electromagnetic characterization of silicon-based coatings. Findings indicated that increasing magnetic additive content enhanced dielectric and magnetic losses, with complex permeability and permittivity spectra rising linearly with the ferrite volume fraction. De Souza Pinto et al. [8] further emphasized how morphology, structure, and filler weight fraction influence the electromagnetic performance of MnZn ferrite/epoxy compounds, proposing strategies to manage absorption and shielding capabilities.

In the context of sea multipath effects, Watts [9] highlighted the ongoing challenge of detecting small targets against sea clutter, which remains a critical concern for operations in littoral environments. Tao [10] proposed a mathematical model to analyze signal fading mechanisms caused by multipath, incorporating stochastic variations (jitter) from recorded radar data. Yang [11] reviewed radar detection techniques for low-altitude targets over water, focusing on multipath scattering environments and strategies such as high-resolution range profiling (HRRP), spatial diversity, and frequency/polarization diversity. However, this analysis is limited to fixed-target radar cross-section (RCS) scenarios (0.1 m^2), lacking dynamic target considerations.

Regarding fluctuating RCS, Wen [12] developed a method to evaluate changes in RCS due to cruise missile attitude variations versus time, using a static RCS database combined with motion trajectory data. However, this model simplifies the missile as a perfect electric conductor and evaluates it at a single frequency (3 GHz), limiting its applicability.

In parallel with developing novel functional materials for stealth applications, there has been a growing emphasis on using computational intelligence and metaheuristic optimization methods in designing aerospace structures and multifunctional systems. Studies employing techniques such as the bees algorithm, genetic optimization, and vibration-based criteria have demonstrated their value in improving the performance of composite shells, smart sandwich plates, and layered nanocomposites under complex thermal and mechanical loads [13–15]. Although initially applied to the structural and energy domains, these strategies offer a compelling foundation for the evolution of electromagnetic material design frameworks, particularly for tailoring radar-absorbing composites with competing performance objectives such as absorption depth, bandwidth, and mechanical compatibility.

To the best of our knowledge, this is the first study to integrate the processing and experimental characterization of MnZn ferrite/epoxy RAM with full-scale electromagnetic and operational simulations tailored to long-range cruise missile applications. Complex permittivity and permeability measurements validated the RAM supported by Lorentz-based dispersion modeling, and high-fidelity simulations of a representative missile geometry quantified effects on radar cross-section (RCS). A dynamic radar detection algorithm was also implemented, accounting for time-varying RCS and sea-surface multipath effects. The results demonstrate that coupling RAM with trajectory optimization can markedly reduce detection range and extend reaction time. The central contribution of this work is a unified stealth framework that bridges materials science, computational electromagnetics, and operational doctrine by combining MnZn/epoxy RAM coatings with adaptive multipath-exploiting flight trajectories. This approach thereby delivers measurable operational advantages-up to −23 dB peak RCS reduction and a 94-s extension in radar reaction time under naval detection scenarios advancing adaptive RF low-observability doctrines and methods for next-generation aerial platforms.

2. Theoretical analysis

2.1. Radar-absorbing material (RAM) basic theory

When a radar emits electromagnetic waves, part of the incident RF energy on a composite material is back-scattered or transmitted through surface waves. At the same time, material absorbs the remainder. RF waves entering the RAM undergo multiple internal reflections, leading to attenuation and conversion primarily into heat [16]. Impedance matching enables a greater portion of the incident energy to enter the structure, reducing surface reflection. The reflection coefficient Γ at the interface between two media is given by:

$$\Gamma = \frac{Z_2 - Z_1}{Z_2 + Z_1} \tag{1}$$

where Z_1 is the impedance of free-space ($\cong$ 377 Ω) and Z_2 is the impedance of the absorbing material [17].

When $|Z_1/Z_2| \to 1$, the RAM enables entry of practically all the incident energy. It should also be noted that Z_2 can be expressed as:

$$Z_2 = \sqrt{\frac{\mu_r}{\epsilon_r}} = \sqrt{\frac{\mu_r' - j\mu_r''}{\epsilon_r' - j\epsilon_r''}} \tag{2}$$

where μ_r and ϵ_r are the complex permeability and permittivity of the absorbing material, μ_r' and ϵ_r' are the real parts representing the capacity of energy storage of the magnetic and electric field; μ_r'' and ϵ_r'' are the imaginary parts related to magnetic and electric field losses, respectively [18].

2.2. Radar cross-section (RCS) and radar range equation

RCS (σ) is defined as a measure of the magnitude of the scattered electromagnetic (EM) wave from a body relative to the magnitude of the wave incident on the body and can be expressed as:

$$\sigma = \lim_{R \to \infty} 4\pi R^2 \frac{|\boldsymbol{E}_s|^2}{|\boldsymbol{E}_i|^2} \tag{3}$$

where R is the distance between the radar and the target, $\boldsymbol{E}_s$ means the scattered electric field strength at the distance R, and $\boldsymbol{E}_i$ is the incident electric field strength at the target [19].

In RF LO applications, minimizing the reflection coefficient ($\Gamma \to 0$) is essential, as it reduces the RCS and thus the radar detection range. The radar range equation under free-space conditions describes the behaviour:

$$R = \sqrt[4]{\frac{P_t (G)^2 (\lambda)^2 \sigma}{(4\pi)^3 L P_r}} \tag{4}$$

where P_t is the transmission power, G is the antenna gain, λ is the wavelength, σ is the target RCS, L are the atmospheric and system losses, R is the detection range, and P_r is the received power at the radar antenna [20].

The RCS depends on several key factors [21]:

- the relative position and orientation between the radar and target;

- electrical properties of the target;
- frequency and polarization of the transmitted wave.

Among all variables in the radar range equation, only σ can be controlled by the target designer; all other factors are dictated by the radar system itself. Designing low-observable missiles involves balancing trade-offs in size, weight, range, payload, and cost. Each of these impacts the final RCS and influences its survivability performance [22].

2.3. Multipath theory

2.3.1. Geometry for multipath propagation

Early warning radars scanning the horizon for sea-skimming missiles at low grazing angles receive the target echo via two distinct paths: a direct path from radar to missile and a reflected path off the sea surface, Fig. 1.

The combined effect of these two paths mimics a virtual image, as if the radar is observing two targets — one real and one reflected below the surface. This phenomenon can introduce significant elevation angle errors, degrading radar tracking accuracy. It can even lessen the effectiveness of terrain bounce jamming [23].

Radar beams used for initially detecting missiles at low grazing angles reflect off the sea surface. This reflection results in a 180° phase shift, with a magnitude of approximately one. The signal reflected from the sea surface is known as the multipath signal, which can cause significant destructive interference with the direct path signal. Such destructive interference is common in low grazing angle search radars and is referred to as multipath error; it can lead to serious inaccuracies in elevation, loss of tracking due to a reduced signal-to-noise ratio (SNR), and disrupt elevation coverage, resulting in a lobed structure.

2.3.2. Smooth surface reflection coefficient

When radar waves reflect off the surface of the Earth, they experience a loss in amplitude and a phase shift [21]. The reflection coefficient depends on the grazing angle, frequency, and polarization of the signal, the divergence factor due to the curvature of the Earth, and the characteristics of the reflecting surface.

The first factor that affects the complete reflection coefficient is the smooth surface reflection coefficient, which assumes a flat surface and, thus, no scattering. The smooth surface reflection coefficient depends upon the polarization and carrier frequency, the dielectric coefficient of the reflection surface, and the radar grazing angle. The reflection coefficients for both vertical and horizontal polarization are calculated by:

$$\Gamma_v = \frac{\epsilon_r \sin\theta_g - \sqrt{\epsilon_r - (\cos\theta_g)^2}}{\epsilon_r \sin\theta_g + \sqrt{\epsilon_r - (\cos\theta_g)^2}} \tag{5}$$

$$\Gamma_h = \frac{\sin\theta_g - \sqrt{\epsilon_r - (\cos\theta_g)^2}}{\sin\theta_g + \sqrt{\epsilon_r - (\cos\theta_g)^2}} \tag{6}$$

where ϵ_r is the complex permittivity of the sea water and θ_g is the RF wave grazing angle. It should be noted that the complex permittivity of the sea water is a function of the incident wave frequency, water temperature, and salinity [21]. Sea water complex permittivity empirical values are available in Refs. [21,24]. Fig. 2 shows the real and imaginary parts of the sea water permittivity under salinity and temperature variations at X-band (8–12 GHz).

Fig. 3 depicts the reflection coefficient magnitude and phase for

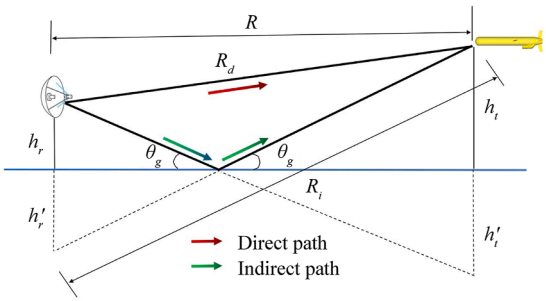

Fig. 1. Geometry of multipath.

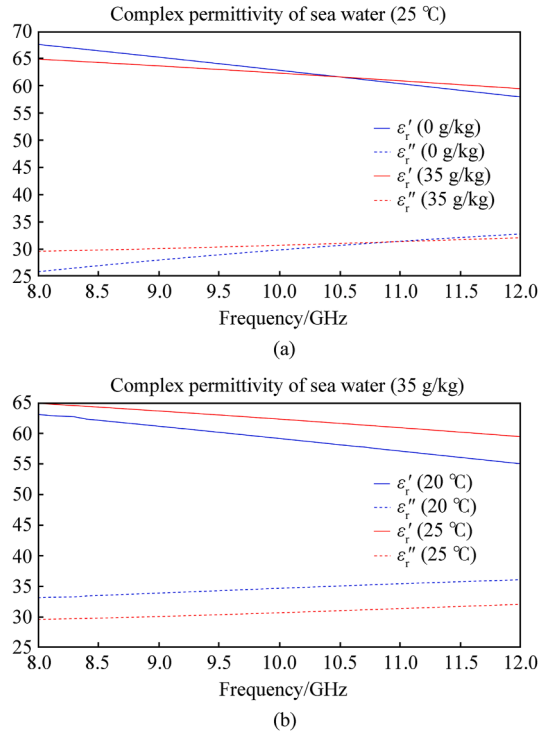

Fig. 2. Complex permittivity of sea water over frequency 8 GHz–12 GHz: (a) Complex permittivity of sea water (25 °C); (b) Complex permittivity of sea water (35 g/kg).

sea water at 20 °C, salinity of 35 g/kg, where $\epsilon_r' = 59.57$ and $\epsilon_r'' = 34.55$ at 9.8 GHz. The plots shown in these figures show the typical general behaviour of the reflection coefficient.

2.3.3. Divergence factor

The complete reflection coefficient is also affected by the spherical-earth divergence factor D, and its formulation is well described by Mahafza [21]. When an electromagnetic wave reflects off the Earth's surface, the reflected wave diverges due to the Earth's curvature. This divergence results in a decrease in reflected power as the energy disperses. The current work concentrates on the detection conditions of a long-range cruise missile at the limits of the radar horizon; thus, the analysis is restricted to the flat-earth model, with D assumed to be 1.

2.3.4. Surface roughness

The third factor included in the reflection coefficient is the surface roughness. Surface roughness, denoted as S_r, is expressed as follows:

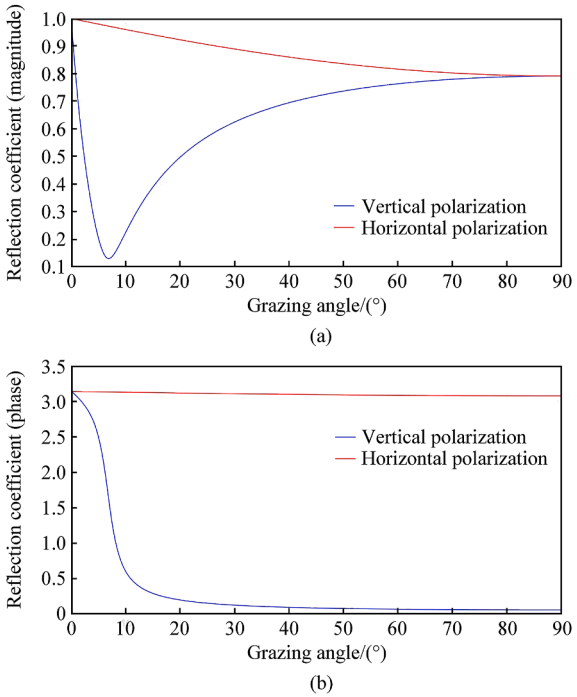

Fig. 3. Reflection coefficient of sea water at 9.8 GHz (20 °C - 35 g/kg): (a) Reflection coefficient magnitude; (b) Reflection coefficient phase.

$$S_r = \exp\left[-2\left(2\pi h_{rms}\sin\theta_g(\lambda)^{-1}\right)^2 \right] \tag{7}$$

where h_{rms} represents the rms surface height. The roughness of the sea is typically defined by the sea-state, which is influenced by the wave height [25,26].

Finally, by combining the three aforementioned factors, the overall reflection coefficient Γ_t can be expressed as follows:

$$\Gamma_t = \Gamma_{h,v}\ D\ S_r \tag{8}$$

here, $\Gamma_{h,v}$ is the vertical or horizontal smoothed surface reflection coefficient.

2.3.5. Pattern propagation factor

Near the Earth's surface, multipath effects dominate the propagation factor. Essentially, the pattern propagation factor describes the destructive and constructive interference patterns of RF waves diffracted off the Earth's surface. This diffraction affects the overall signal strength at the target by the ratio of the signal strength in the presence of the Earth to the signal strength at the target in free space. The pattern propagation factor F_p is computed as:

$$F_p = \sqrt{1 + (\rho)^2 + 2\rho\cos\alpha} \tag{9}$$

where ρ is the indirect signal amplitude and α is the phase shift induced by the difference between the two paths, plus the effect of surface roughness. It follows that the signal power at the target is modified by the factor F_p^2 [21]. By using reciprocity, the received signal power at the radar is computed by multiplying (4) by the factor F_p^4. Fig. 4 shows a comparison between the received signal from a target flying at a fixed altitude, considering and not the pattern propagation factor.

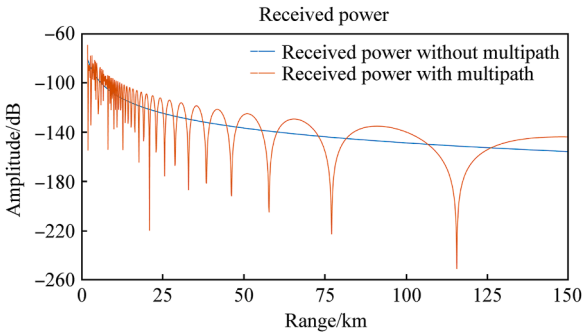

Fig. 4. Effect of multipath on radar received power (flat-earth model).

3. Methodology

Fig. 5 illustrates the workflow and methodology employed in this study.

The overall methodological framework was structured in four sequential and interdependent stages, as illustrated by the blue blocks in Fig. 5. Each stage feeds the next through physically measurable quantities, ensuring that numerical and operational simulations remain grounded in experimental reality.

(1) Stage I — Sample Preparation. This stage defines the fabrication protocol for the MnZn ferrite/epoxy composites, controlling filler proportion, curing parameters, and specimen geometry. The objective is to obtain homogeneous and dimensionally stable coupons compatible with standard waveguide testing in X-band.

(2) Stage II — Measurement Techniques (Reproducibility). The purpose here is to ensure material reproducibility and validation of the composite's electromagnetic behaviour. Morphological and structural integrity of the ferrite phase and the epoxy resin are verified by FEG-SEM/EDS, Raman spectroscopy, FT-IR, and XRD while scattering parameters are measured in vector network analyzer. From the experimental *S*-parameters, the complex permittivity $\varepsilon_r(f)$ and permeability $\mu_r(f)$ are retrieved, establishing a reproducible electromagnetic fingerprint for the manufactured composite.

(3) Stage III — Electromagnetic Simulation. The experimentally obtained *S*-parameters provide the transition link between the laboratory and the computational domains: the measured $\varepsilon_r(f)$ and $\mu_r(f)$ are imported into the FEKO® material library to reproduce the composite's response in simulation. The RAM behaviour is first analyzed on a flat-plate model to isolate the effects of angular incidence and polarization sensitivity under simple boundary conditions. This baseline step verifies how the absorber responds to variations in grazing angle and incident-field polarization. Subsequently, the coating is applied to a complex geometry—the BGM-109 cruise-missile model—to capture multi-faceted scattering mechanisms, including wedge/edge diffractions. This progression (planar → complex) separates material effects from purely geometric contributions and validates that improvements observed in canonical targets translate to realistic airframes.

(4) Stage IV — Radar-Detection Simulation. The RCS data from the complex-geometry analysis are compiled into a dynamic loading matrix that feeds the MATLAB®-based naval radar detection algorithm. This step performs a physically consistent field-level analysis that emulates operational

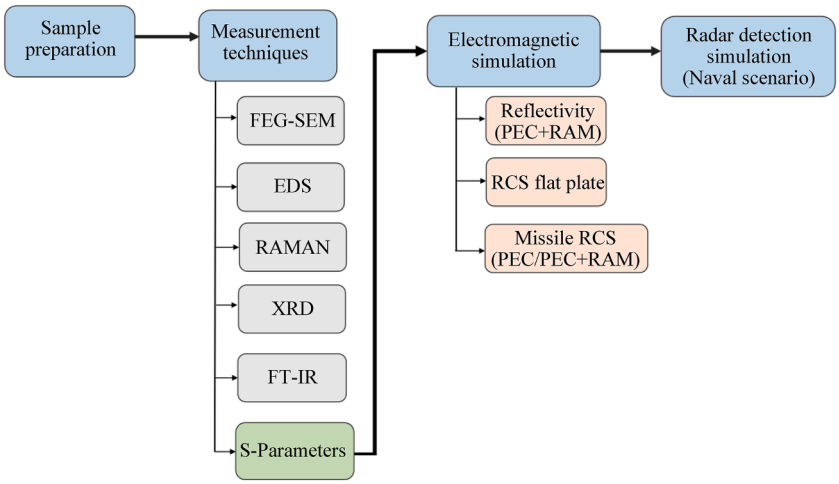

Fig. 5. Activities workflow.

engagement conditions at a fraction of the cost and logistical complexity of full-scale trials. From an assessment standpoint, the simulated RCS database provides a parametrically consistent substitute for instrumented range campaigns, with material fidelity ensured by the Stage II–III calibrated $\varepsilon_r(f)$ and $\mu_r(f)$.

Together, these four stages close the experimental-to-operational loop by (i) fabricating and characterizing the absorber, (ii) reproducing it numerically with measured ε_r and μ_r, (iii) evaluating its performance from planar to complex targets (including polarization and diffraction phenomena), and (iv) quantifying tactical implications via radar-detection modeling.

3.1. Sample preparation

To support reproducibility, this section details the preparation protocol, material proportions, and curing parameters for the MnZn ferrite/epoxy composites. We made a fast-curing epoxy coating by mixing resin and the hardener in a 50:50 mass ratio. The magnetic filler used was $Mn_{0.58}Zn_{0.42}Fe_2O_4$ (MnZn ferrite) powder as a filler for the matrix. Composite samples were fabricated with thicknesses of 4 mm and 5 mm, while reference samples of pure epoxy resin were prepared under the same conditions but without the filler. For the composite preparation, we mixed the MnZn ferrite powder into the epoxy mass before and after adding the hardener. Once homogenized, the mixture was poured into silicone molds to form rectangular pellets measuring 10.16 mm by 22.86 mm, ensuring a precise fit within the X-band WR-90 waveguide. Ferrite concentrations of 50 wt%, 60 wt%, and 70 wt% (relative to the total mass of resin and hardener) were investigated. Each condition was reproduced in triplicate, totaling eighteen samples, with reflection coefficient magnitude root mean square (rms) errors below 1.3 dB.

Additional process characterization was conducted to document the manufacturing protocol further and verify fabrication consistency. The resin and catalyst masses were precisely weighed at approximately 2.0 g and 1.0 g, respectively, prior to ferrite addition. The MnZn ferrite powder was incorporated at 50 wt%, 60 wt%, and 70 wt% relative to the total resin-catalyst mass (approximately 3.0 g). For each composition, the ferrite was initially homogenized into the resin under slow agitation to promote uniform dispersion, followed by the addition of the catalyst and continued homogenization, resulting in a total mixing time of approximately 5 min per sample. The final mixtures were cast into WR-90-conforming silicone molds (4 mm and 5 mm thickness), which had been pre-treated with carnauba wax to facilitate sample extraction after curing. The samples were cured under ambient conditions at room temperature (25 °C) for 24 h to ensure full crosslinking of the epoxy matrix.

Mass density measurements were conducted across all specimens to support the assessment of fabrication reproducibility. The average measured density was 3.44 g/cm^3, confirming the preparation method's consistency and the processing parameters' stability. An example of the fabricated composite is presented in Fig. 6, illustrating the surface finish and dimensional uniformity achieved.

3.2. Measurement techniques

3.2.1. FEG-SEM/EDS

We performed morphological analysis and elemental composition mapping of the MnZn ferrite powder using a Tescan Mira 3 field emission scanning electron microscope (FEG-SEM) coupled with energy-dispersive X-ray spectroscopy (EDS). The measurements used a 10 mm and 15 mm working distance, 100× and 500 × magnification, and 5 kV accelerating voltage to ensure optimal image resolution from four different regions.

3.2.2. Raman spectroscopy

Raman analysis was conducted with a Horiba Scientific LabRAM HR Evolution system to confirm the presence of MnZn ferrite and rule out α-Fe_2O_3 impurities, which negatively affect magnetic behavior. The setup employed a 514.5 nm laser with

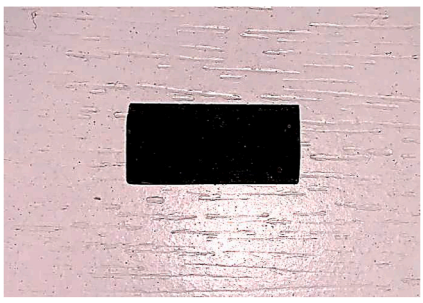

Fig. 6. Manufactured MnZn ferrite/epoxy sample.

20 × magnification and a spectral range of 100–1000 cm^{-1}.

3.2.3. XRD

We used X-ray diffraction (XRD) to complement Raman analysis and verify the ferrite's crystal structure. The measurements were taken using a Rigaku Ultima IV diffractometer with CuK α X-ray (α = 0.154 nm). Scans covered the 2θ range from 16° to 90°, with a step size of 0.02° and a 10 s counting time. This setup was optimized for the micrometric scale and crystallographic characteristics of MnZn ferrite. The wide angular range enabled detection of all relevant planes in the spinel cubic structure, while high resolution and long acquisition time improved signal-to-noise ratio. These conditions allowed accurate phase identification and crystallinity assessment, including the detection of weak or overlapping peaks.

3.2.4. FT-IR

We characterized the cured epoxy matrix using Fourier-transform infrared spectroscopy (FT-IR). A Frontier PerkinElmer spectrometer operated in UATR mode (0.8 mg analyte/400 mg matrix) in the medium infrared (4000–400 cm^{-1}) region. This configuration minimizes humidity effects and enables reliable spectral interpretation.

3.2.5. Scattering parameters

We evaluated the scattering parameters (S_{11}, S_{12}, S_{21}, and S_{22}) and complex permittivity and complex permeability at X-band frequencies (8.2–12.4 GHz) of the MnZn ferrite/epoxy (composite) samples using a vector network analyzer (VNA Keysight®, model N5232A, test set WR-90), Fig. 7. From the experimental S-parameters, the complex parameters of ϵ_r and μ_r were determined using the software 85071E from Keysight®, based on the Nicolson-Ross model [27].

To measure microwave absorption, the reflectivity Γ is determined by S_{11}, both in magnitude and phase [28]. The reflection loss *RL* is based on a model of a single-layer plane wave absorber and is given by:

$$RL = -20\log_{10}(|S_{11}|) \tag{10}$$

3.3. Electromagnetic simulation

All electromagnetic simulations were performed using FEKO® software, employing both transmission/reflection analysis and RCS modeling to assess the electromagnetic behaviour of the MnZn/epoxy composite.

Initially, the measured reflection and transmission coefficients of the actual composite material were used to validate the simulated material dielectric properties (complex permittivity and permeability) as this was reproduced in FEKO®. This ensured consistency between the numerical model and real sample behaviour, serving as a foundation for free-space simulations.

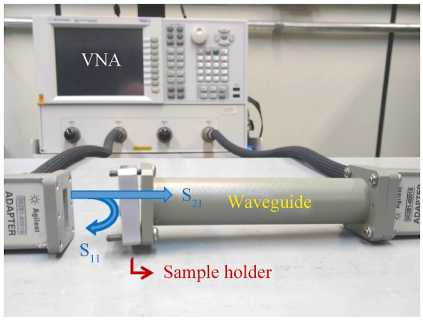

Fig. 7. Electromagnetic measurements setup (VNA, waveguide, and a WR-90 type sample holder).

Subsequently, a flat metallic plate (10 cm × 10 cm) was modeled and illuminated at varying azimuthal angles and different linear polarizations (vertical-vertical, VV, and horizontal-horizontal, HH) to evaluate the reflectivity reduction under idealized conditions. The same composite coating (MnZn ferrite/epoxy) was then applied to a 3D model of a typical long-range cruise missile. The Raytheon BGM-109 Tomahawk was used as a baseline 3D model. Fig. 8 illustrates the real and 3D-modeled geometries. RCS simulations were carried out under monostatic conditions using two complementary numerical methods:

- the Method of Moments (MoM) for the flat plate configuration, suitable for smaller structures;
- the Ray-Launching Geometrical Optics (RL-GO) asymptotic method for the missile model, which is appropriate for electrically large bodies exceeding 20λ [29]. FEKO integrates the RL-GO method with the current-based MoM, by launching rays from each radiating MoM element.

The RL-GO solver is a high frequency method similar to the Shooting and Bouncing Rays (SBR). The method uses ray-tracing from the emitter, bouncing within the geometry surface, represented by a triangular mesh, and following the Geometrical Optics (GO) rules until they leave to the infinity [30]. Furthermore, it is capable of reproducing the effects of wedge/edge diffractions.

All RCS calculations assumed far-field conditions, and surfaces were modeled as perfect electric conductors (PEC) and PEC with RAM coating, allowing direct comparison of LO performance.

Two representative frequencies were selected: 9.3 GHz and 9.8 GHz. These frequencies were chosen not only because they lay within the ITU radio-location allocated bands [31], but also because they cause diffraction effects, since shorter wavelengths are of comparable size to the missile's surface protuberances [19].

To support radar detection simulations, a RCS database was generated from angular scans ranging from 0° to 180° in azimuth and elevation, with an angular step of 0.1°. This is justified because the angular step (in radians) depends on the maximum size *L* of the target and the minimum carrier frequency:

$$\Delta\phi = \lambda/2L \tag{11}$$

This database captured the complete angular pattern of the target's signature for dynamic detection, discussed in the following section.

3.3.1. Software validation

The numerical procedure was validated using the PEC NASA almond 3D model [32]. Experimental data were compared at 1.19 GHz and 7 GHz, conducted in both horizontal (HH) and vertical (VV) polarizations. The results are shown in Fig. 9. At a frequency of 1.19 GHz, Fig. 9(a), the simulations accurately predicted RCS in both VV and HH polarizations. Similarly, at the higher frequency, Fig. 9(b), is in good agreement with the experimental data in both polarizations.

Mesh convergence was validated for the BGM-109 geometry in X-band (9.8 GHz). Three meshes were developed: coarse, standard, and fine. Table 1 presents the mesh parameters. Additionally, in the RL-GO solver settings, the maximum number of ray interactions was set to six, ensuring that multiple reflections and diffractions were captured without excessive computational overhead.

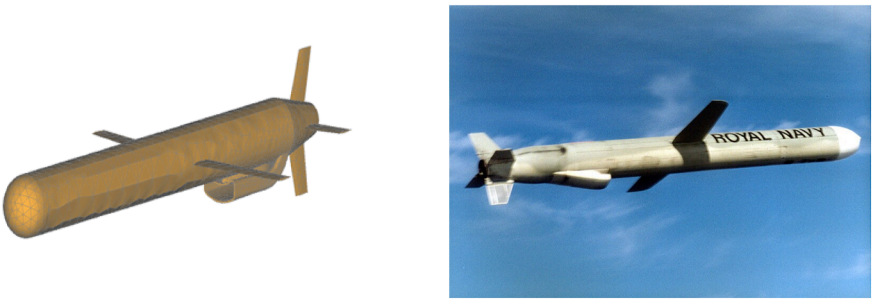

Fig. 8. BGM-109 CAD/real model (length: 5.56 m, diameter: 0.52 m, wingspan: 2.67 m).

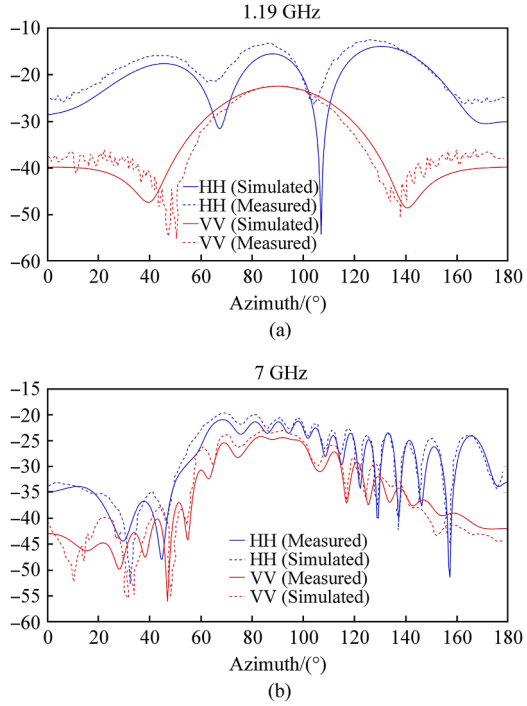

Fig. 9. 3D NASA metallic almond benchmark: (a) 1.19 GHz 3D NASA almond; (b) 7 GHz 3D NASA almond.

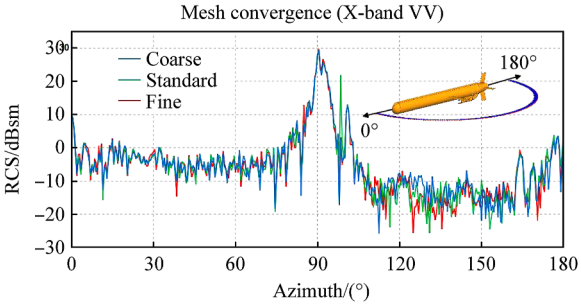

Fig. 10. X-band mesh convergence.

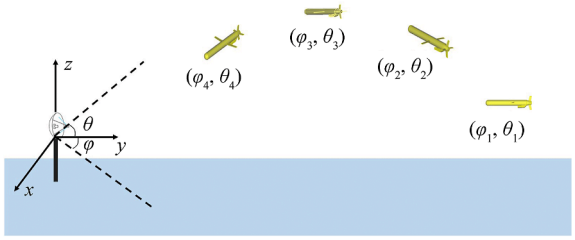

Fig. 11. Radar detection scenario.

Table 1
Mesh parameters.

Mesh type	Number of triangle splines	Average edge length
Coarse	10,372	3.78 cm
Standard	11,836	3.59 cm
Fine	44,136	2.57 cm

In Fig. 10, the deviation between the three meshes indicates that the standard mesh yielded a grid-converged solution.

3.4. Radar detection simulation (naval scenario)

The scenario, developed in MATLAB®, examined a frequency diverse naval radar to detect a long-range cruise missile. The target can manoeuvre in azimuth (φ) and elevation (θ). The analysis focuses on the lobbing effect produced by the sea multipath and how the RAM coating can delay detection. The algorithm integrates the EM wave specular reflection and phase-shift effects over the sea surface with the missile's dynamic (time-varying) RCS. This is constrained only by the radar's pulse repetition frequency (PRF) due to blind ranges and velocities. The latter happens when the Doppler echo lies inside the periodic radar main beam clutter (MBC).

Radar detection simulations were conducted in an ideal, clutter-free environment, where the radar operates at minimum sensitivity for given probability of detection and probability of false alarm. In real-life maritime scenarios, sea clutter and atmospheric attenuation degrade radar performance, particularly at low grazing angles. Therefore, the results presented are conservative, as RAM-coating reduces detection range in realistic conditions [21]. Fig. 11 illustrates the radar detection scenario, and Table 2 lists the input parameters.

Although curved-earth models provide higher fidelity in long-range detection simulations, the flat-earth approximation is widely adopted for naval radar scenarios up to 100 km. In this range, the dominant limiting factor is the radar horizon, which is primarily depends on the radar antenna and target elevation. Since this study focuses on sea multipath interference and radar detection performance, the flat-earth model offers sufficient fidelity and significantly reduces computational complexity [26]. Additionally, atmospheric attenuation needs to be accounted for radar frequencies beyond 8 GHz, thus affecting detection at the radar horizon [21]. Fig. 12 shows the radar detection algorithm flowchart:

Table 2
Scenario input parameters.

Operating radar frequencies	9.3/9.8 GHz
Radar height	35 m
Pulse width	0.24 μs
Peak power	70 kW
Pulse repetition frequency (PRF)	1800 Hz
Polarization	VV
Beamwidth	1.4°
Antenna gain	33 dB
Antenna rotation	6 RPM
Integration efficiency	80%
Probability of detection (P_d)	50%
Probability of false alarm (P_{fa})	10^{-5}
Total system and atmospheric losses	9 dB
Receiver noise figure	5.3 dB
Sea state/temperature	1/3/4 (20 °C)
Sea Salinity	35 g·kg^{-1}
Missile speed ($v_{missile}$)	192 m·s^{-1}
Missile flight level	Low (2 m)/High (300 m)

4. Results and discussion

4.1. FEG-SEM/EDS

The MnZn ferrite microstructure and its particle size distribution are shown in Fig. 13. Scanning electron micrograph (SEM) images of fractured particles show acicular and plate shaping. An average grain size of 20.62 μm and a standard deviation of 14.76 μm can be estimated from the image. This microstructural heterogeneity has a direct impact on the electromagnetic performance of MnZn/epoxy composites. Fine particles and irregular shapes enhance interfacial polarization and create additional conduction pathways within the epoxy matrix, thereby increasing dielectric loss [33]. Larger grains favor domain-wall resonance and natural magnetic resonance in the GHz range, reinforcing magnetic loss. Finally, the broad particle size distribution ensures multiscale relaxation times, which contributes to improved impedance matching over a wider frequency band.

Table 3 shows the EDS analysis results of the MnZn ferrite additive.

4.2. Raman spectroscopy

Fig. 14 shows the MnZn ferrite Raman spectrum. After deconvolution, one can observe a broad, low-intensity 1st order local maximum at approximately a wavenumber of $k = 345$ cm^{-1}. This is associated with an E_g mode that corresponds to a doubly degenerate symmetric vibration, which is typically associated with planar oxygen displacements within the octahedral sites of

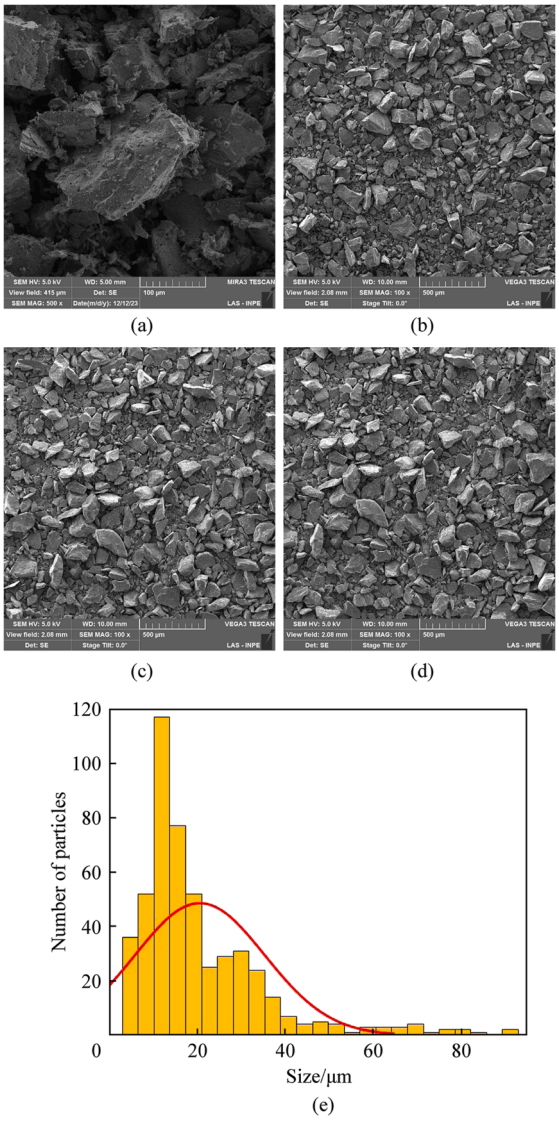

Fig. 13. FEG-SEM images and particle size distribution: (a) SEM image region 1; (b) SEM image region 2; (c) SEM image region 3; (d) SEM image region 4; (e) Particle size distribution.

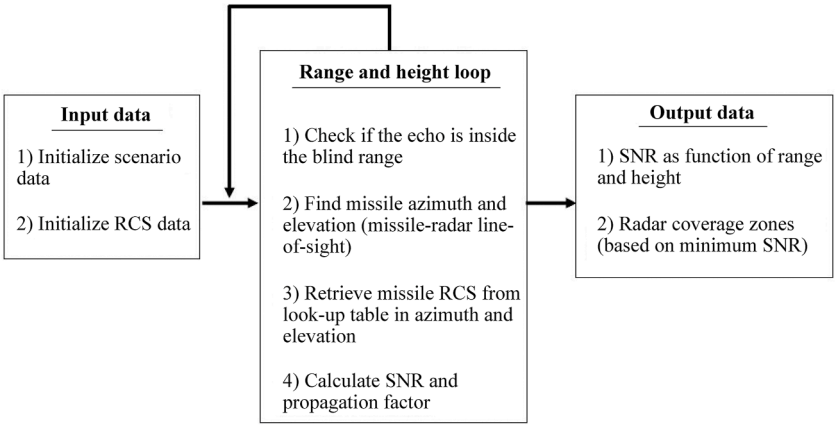

Fig. 12. Radar detection algorithm flowchart.

Table 3
MnZn ferrite chemical elemental composition.

Element	Weight/%
C	2.3
O	28.8
Fe	50
Mn	12.1
Zn	6.8

the spinel lattice. The presence of α-Fe_2O_3 impurity is ruled out, as this phase shift produces a local maximum at approximately $k = 245$ cm^{-1}. The absence of α-Fe_2O_3 local maxima in the Raman spectrum is a desirable result, as this phase shift typically acts as a non-magnetic impurity in MnZn ferrites. The presence of α-Fe_2O_3 local maxima can reduce the magnetic permeability, thus compromising the overall microwave absorption of the composite [34].

At approximately k = 625 cm^{-1}, 729 cm^{-1}, and 785 cm^{-1}, three stretching modes are observed. These correspond to tetrahedral coordination from the Mn-O, Zn-O, and Fe-O molecular bonds, respectively [35].

4.3. X-Ray Diffraction (XRD)

Fig. 15 presents the XRD analysis of the MnZn ferrite diffraction pattern, which displays a cubic crystal structure and Fd-3m vibrational mode characteristic of the spinel cubic structure. A strong correlation was observed with other MnZn ferrites reported in the literature and the crystallographic pattern [36–38].

4.4. FT-IR

Fig. 16 shows the infrared (IR) spectroscopy of the cured epoxy resin. The spectrum reveals the presence of diglycidyl ether of bisphenol A (DGEBA) resin, with a C-O deformation local maximum centered at $k = 915$ cm^{-1}, C–H stretching of the terminal oxirane group at $k = 3050$ cm^{-1}, and the characteristic maximum of O–H stretching of hydroxyl groups at $k = 3500$ cm^{-1} [39,40].

4.5. Scattering parameters

4.5.1. Pure epoxy resin complex permittivity and permeability

Figs. 17 and 18 show the X-band variations of real and imaginary parts of the complex permittivity and permeability for 4 mm and 5 mm thick epoxy samples. These data serve as a baseline to compare the electromagnetic behaviour of the pure epoxy matrix against the composite samples, particularly highlighting the absence of significant magnetic response and the stability of dielectric properties across X-band.

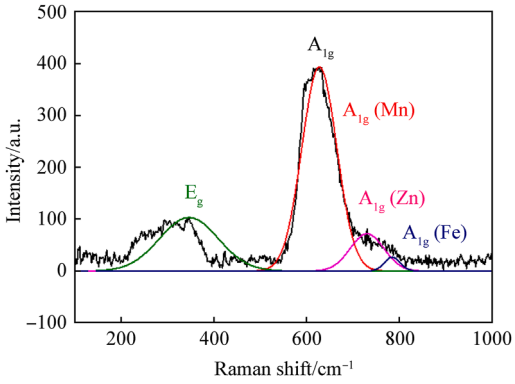

Fig. 14. MnZn ferrite Raman spectroscopy.

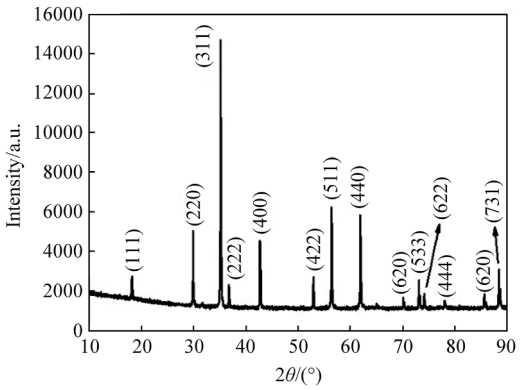

Fig. 15. XRD analysis of MnZn ferrite.

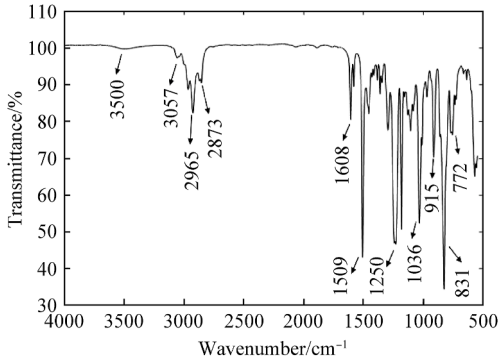

Fig. 16. Epoxy resin (DGEBA) FT-IR in the MIR range.

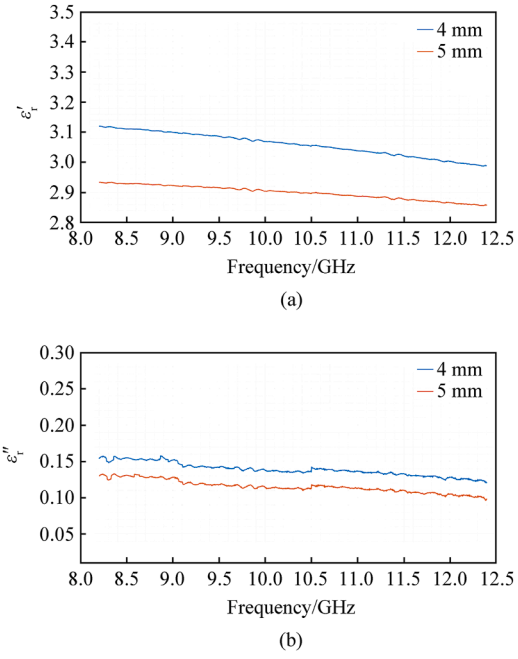

Fig. 17. Complex permittivity of pure epoxy resin samples: (a) Real part of complex permittivity of pure epoxy resin; (b) Imaginary part of complex permittivity of pure epoxy resin.

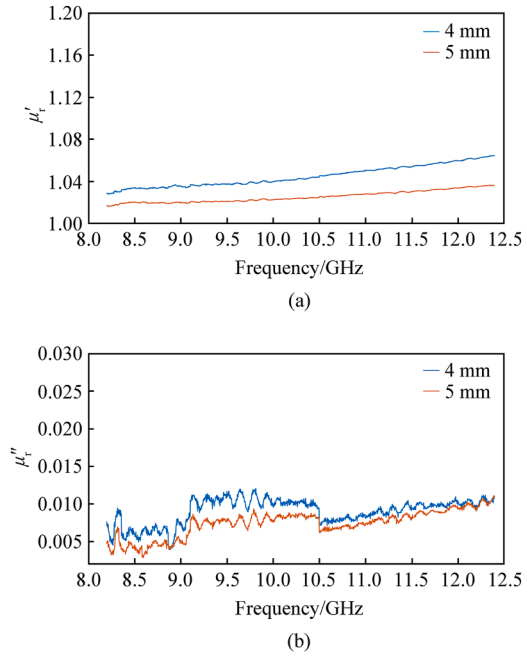

Fig. 18. Complex permeability of pure epoxy resin samples: (a) Real part of complex permeability of pure epoxy resin; (b) Imaginary part of complex permeability of pure epoxy resin.

From the analysis of Figs. 17 and 18, it can be seen that the pure epoxy matrix exhibits a purely dielectric response, with minimal variation in permittivity and negligible variation in permeability versus sample thicknesses and frequency.

4.5.2. MnZn/epoxy complex permittivity and permeability

Figs. 19 and 20 show the X-band variations of real and imaginary parts of the complex permittivity and permeability for all MnZn/epoxy samples.

From the analysis of Fig. 19(a), inserting a magnetic additive into the epoxy matrix proportionally increases the dielectric constant with regard to resin mass, up to approximately 9 GHz. Hence, the insertion of the magnetic additive increases the capability of the material to store energy. Such behavior is typical in heterogeneous dielectric materials, where mismatches in permittivity between layers lead to inter-layer charge accumulation and enhanced dielectric constant [41,42]. Heterogeneity increases as the magnetic additive is inserted in the epoxy resin, resulting in a greater inter-layer area, and thus greater capacitance [43]. This frequency-dependent behaviour reflects a shift from co-polar backscatter to frequency dependent resonance, as predicted by the Lorentz model, which governs dielectric dispersion in composite systems. This model assumes that electrons in a material behave as harmonic oscillators when excited by an external electric field. An abrupt drop in the real part of permittivity, coupled with an increase its imaginary part, is observed. Hence, the material behaves as a microwave energy absorber [44].

The dielectric loss in Fig. 19(b) spectra shows resonance peaks of dipole dispersion at specific frequencies and correlates with the behaviour of the real part of permittivity. This feature may stem from selective orientation polarization and will be confirmed by reflection loss analysis in Fig. 21. The dielectric curves presented in Fig. 19 exhibit fluctuation peaks at distinct frequencies, reflecting multiple relaxation processes in the MnZn/epoxy composites. These oscillations can be attributed to interfacial polarization and dipolar relaxation arising from the heterogeneous particle size

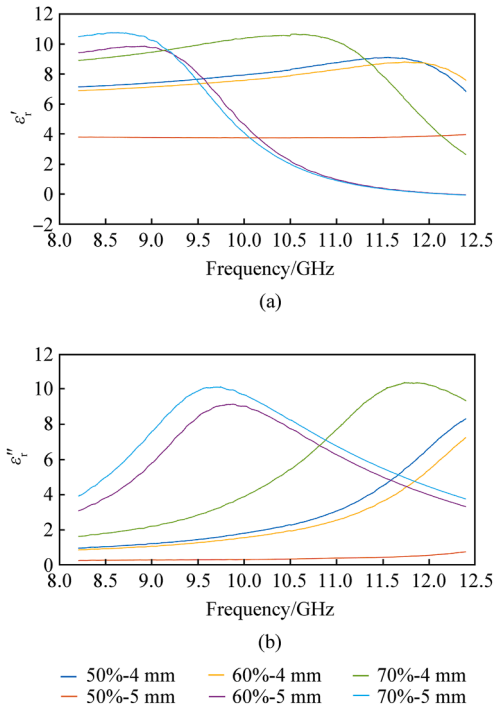

Fig. 19. Complex permittivity of MnZn/epoxy samples: (a) Real part of complex permittivity of MnZn/epoxy samples; (b) Imaginary part of complex permittivity of MnZn/epoxy samples.

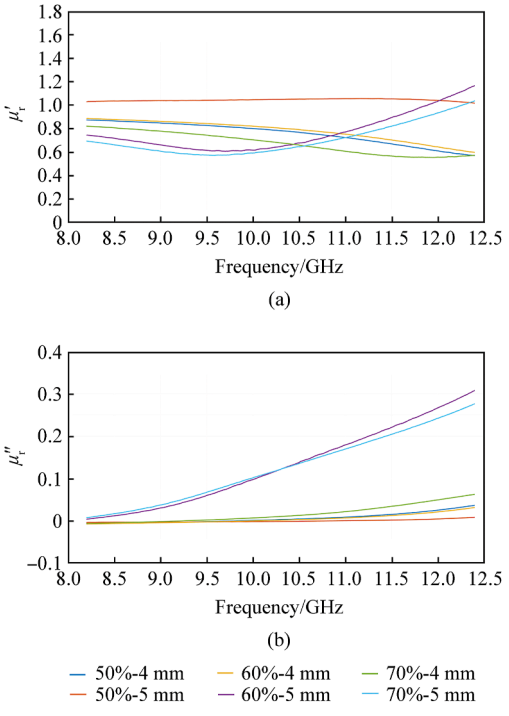

Fig. 20. Complex permeability of MnZn/epoxy samples: (a) Real part of complex permeability of MnZn/epoxy samples; (b) Imaginary part of complex permeability of MnZn/epoxy samples.

distribution and morphology of the ferrite fillers. Similar fluctuation features have been reported in carbon–carbide and rGO-based aerogels, where hierarchical porosity and multi-scale interfaces induce resonance-like peaks in ε' and ε'', directly linked to

enhanced electromagnetic attenuation [45,46].

Regarding complex permeability, Fig. 20 illustrates that increased additive concentrations result in a boost of permeability due to a stronger interaction between the ions' electrons in these sublattices (spin moments and movement of the magnetic domain wall). In this context, the 60%-5 mm and 70%-5 mm samples demonstrated greater magnetic dissipation.

4.5.3. Reflection loss

Fig. 21 confirms the microwave absorption bandwidth, which directly correlates with the permittivity and permeability as previously discussed. As expected, the 50%-5 mm sample exhibited the least significant results, with attenuation ranging from −3.6 dB to −1 dB across the entire frequency range. As discussed, with regards to permittivity and permeability, this sample displayed a substantial prevalence of characteristics typical of the pure epoxy matrix. The 50%-4 mm and 60%-4 mm samples showed virtually identical behaviour, reinforcing previously observed trends from similarities between permittivity and permeability. The 70%-4 mm sample achieved significant absorption, with a peak of −17 dB at 10.8 GHz and a bandwidth of 2.9 GHz, likely due to the synergistic effect of increased polarization and magnetic resonance at that composition.

According to Fig. 21 analysis, the 70%-5 mm and 60%-5 mm samples provided the best results. Notably, both exhibited a synergy between electric and magnetic dissipation effects within their structures, based on the principles of the Lorentz model. The 70%-5 mm sample presented an absorption peak of −22 dB at 9.45 GHz and an effective bandwidth of 1.8 GHz. The 60%-5 mm sample showed an absorption peak of −23 dB at 9.8 GHz and an effective bandwidth of 3.4 GHz.

Table 4 summarizes the results of the reflectivity test for the samples.

The absorption behavior observed in the MnZn/epoxy composites is consistent with recent advances in magnetic–dielectric hybrids where interfacial polarization, defect engineering, and heterostructure design play dominant roles. For example, Wang et al. reported that defect-induced polarization centers in $MoSe_2$/$NiSe_2$@C@PC hybrids significantly enhanced dipolar relaxation and impedance matching [47], while Nan et al. demonstrated that multi-scale porous architectures promote broadband absorption and corrosion resistance in marine-like conditions [48]. Similarly, Xue et al. emphasized that multidimensional heterointerfaces enriched with nitrogen dopants amplify polarization loss and optimize dielectric response in ultrathin absorbers [49], and Wang et al. showed that Schottky barrier engineering at SnS_2/CoNi@NC interfaces establishes internal electric fields that strengthen interfacial polarization and extend bandwidth [50]. In line with these studies, the present work confirms that particle size distribution and morphology of MnZn ferrite synergistically enable conduction loss, interfacial polarization, and impedance matching, culminating in the −23 dB resonance at 9.8 GHz.

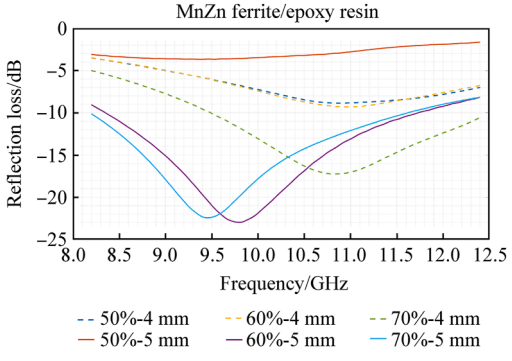

Fig. 21. Reflection loss (RL) of all MnZn/epoxy samples.

Table 4
MnZn/epoxy reflectivity summary. A dash (–) indicates that no absorption bandwidth below −10 dB was observed for the respective composition.

Sample	Maximum RL (frequency)	Bandwidth (<-10 dB)
50%-4 mm	−8.8 dB (10.7 GHz)	–
50%-5 mm	−3.6 dB (9.4 GHz)	–
60%-4 mm	−9.3 dB (11 GHz)	–
60%-5 mm	−23 dB (9.8 GHz)	3.4 GHz
70%-4 mm	−17 dB (10.8 GHz)	2.9 GHz
70%-5 mm	−22 dB (9.45 GHz)	1.8 GHz

For greater accuracy, we selected the 60%-5 mm sample for further study, based on the most significant results with regards to attenuation and bandwidth. Its electromagnetic signature indicates strong impedance matching and balanced wave dissipation, making it an ideal candidate for integration into X-band RF LO structures.

It should be noted that, in practice, RAM coatings rarely achieve perfect thickness uniformity. Variations of ±0.5 mm are common in large-scale applications, and several studies have reported that such non-uniform layers can broaden the effective absorption bandwidth by introducing multiple effective path lengths for the incident wave [51,52]. In the present work, however, we deliberately considered uniform thicknesses, as the study corresponds to a lower Technology Readiness Level (TRL) focused on proof-of-concept validation.

4.6. Electromagnetic simulation

Using the complex permittivity and permeability data for 60% weight fraction and 5 mm thickness sample, the RAM coating was modeled in FEKO®, and the reflection loss, phase shift and impedance (Z_{in}) and phase graphs, Fig. 22, were generated at X-band (8.2 GHz–12.4 GHz).

The impedance spectrum of the 60%-5 mm composite shows a maximum near 9.8 GHz, where the $|Z_{in}|$ becomes predominantly resistive. At the same frequency, the Z_{in} phase exhibits an inversion, which is a well-established signature of resonant behavior. This effect enables efficient dissipation of incident electromagnetic energy and coincides directly with the minimum reflection loss of −23 dB observed at 9.8 GHz. The impedance and phase responses, therefore, confirm that the optimal absorption results from the synergistic effect of conduction and polarization losses balanced under near-matching conditions.

Figs. 23 and 24 show a free-space test simulation where a 10 cm × 10 cm flat plate was designed and its RCS measured versus azimuth (φ), at (9.3/9.8 GHz), and linear polarization (HH and VV).

Finally, axially symmetrical the BGM-109 cruise missile baseline was coated with the MnZn epoxy coating and its RCS was measured versus azimuth and elevation in 0.1° increments, as illustrated in Fig. 25.

Fig. 26 shows the comparative polar graphs between frequencies (9.3/9.8 GHz) and configurations (PEC/RAM-coated).

The RCS was measured at 9.3/9.8 GHz, as shown in Figs. 27 and 28. Using the RCS data from these graphs, a dynamic RCS database was created and used as a loading matrix in the radar detection algorithm.

It is assumed that:

- the radar is trying to detect the missile at low grazing angles (at the extent of the radar horizon);

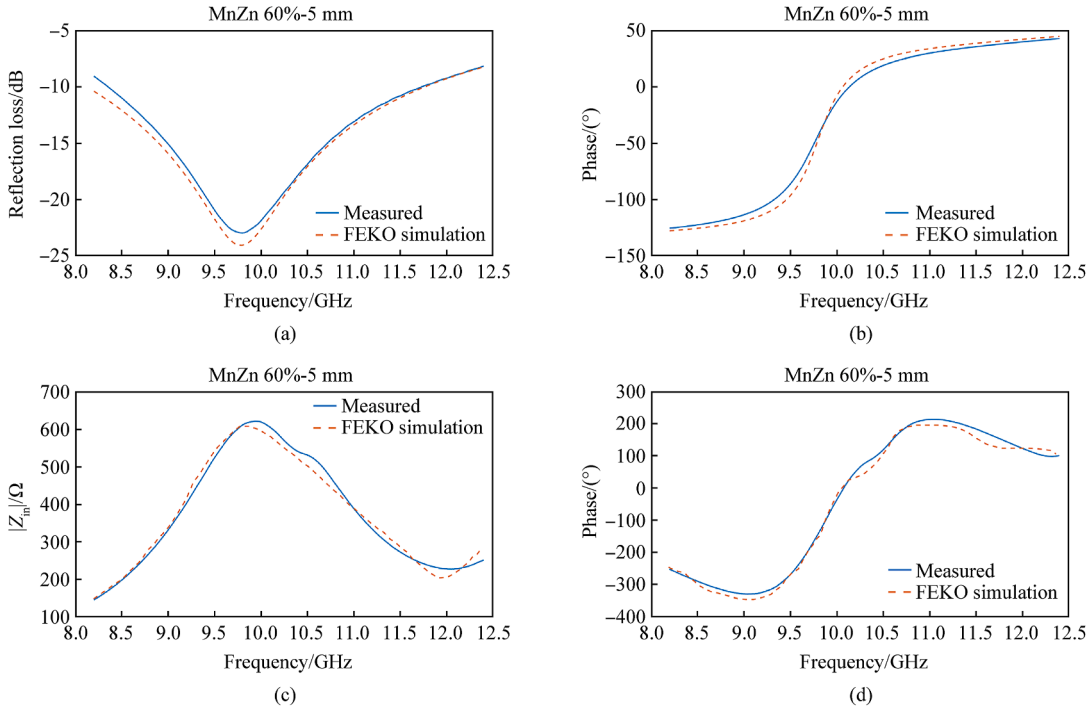

Fig. 22. Reflection coefficient and impedance graphs of MnZn/epoxy sample (60%-5 mm): (a) Reflection coefficient magnitude; (b) Reflection coefficient phase; (c) $|Z_{in}|$ graph; (d) Z_{in} phase graph.

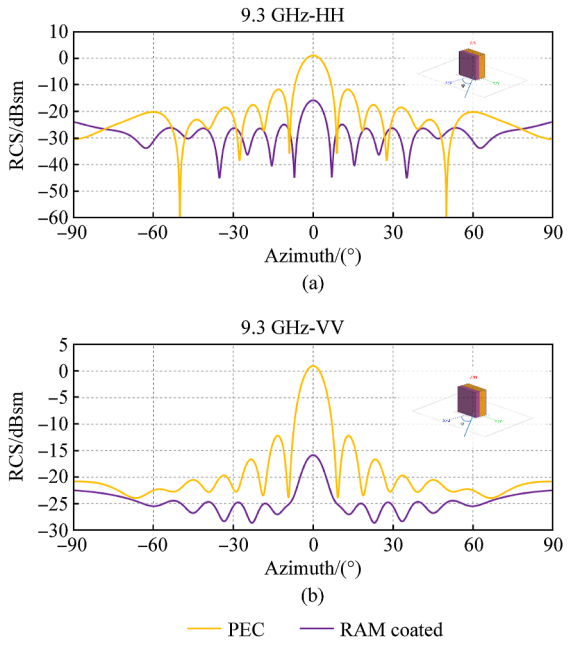

Fig. 23. 9.3 GHz HH/VV flat-plate analysis: (a) RCS comparison of PEC/RAM-coated flat plate (9.3 GHz/HH); (b) RCS comparison of PEC/RAM-coated flat plate (9.3 GHz/VV).

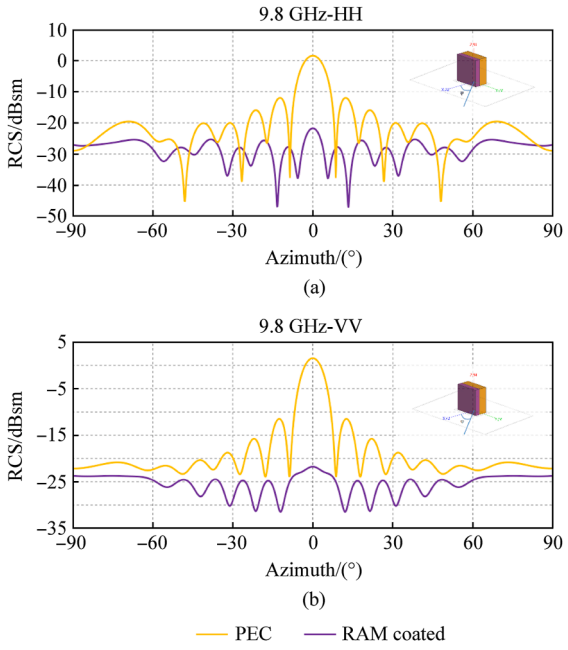

Fig. 24. 9.8 GHz HH/VV flat-plate analysis: (a) RCS comparison of PEC/RAM-coated flat plate (9.8 GHz/HH); (b) RCS comparison of PEC/RAM-coated flat plate (9.8 GHz/VV).

- the cruise missile flies head-on towards the radar.

In Fig. 21, it is observed that the RAM coating suppressed consistently the missile RCS, up to 25.45 dBsm (99.7%), which drastically lowers the missile monostatic radar detectability. For a deeper analysis, it is essential to explore the maps in Fig. 22. Table 5 offers a comparison of RCS variations considering all combinations of azimuth and elevation:

Analysis of Table 5 indicates that the RCS of the BGM-109 baseline spans across a bandwidth of 55 dBsm in both frequencies. In a dynamic detection context, these values will inevitably yield different maximum radar detection ranges. Therefore, all RCS data must be analyzed to extract operational tactics and techniques.

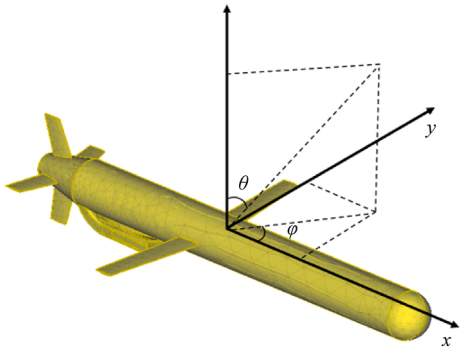

Fig. 25. Azimuth (φ)/elevation (θ) radar illumination.

4.7. Radar detection simulation (naval scenario)

In operational terms, material-level absorption and the resulting airframe-level RCS reductions are explicitly mapped to detection-range changes via the radar-range equation with the multipath propagation factor, $R \propto \left(F_p^4 \sigma\right)^{1/4}$, under the modeled X-band naval radar and sea states (Table 2).

The analysis relies on the head-on missile aspect angle and additionally incorporates representative sea states (1, 3, and 4), which increase the realism of the scenario and provide a decision-making framework of high operational value for naval engagements. Fig. 29 illustrates the profiles for the PEC and RAM-coated configurations (sea state 1). The red areas represent detection zones, while the blue areas signify non-detection zones:

The multipath effect creates RF invisibility lobes where the received power falls below the radar's detection threshold. If the missile's flight profile is tailored to follow one of these null channels, it can approach the target with a lower probability of detection compared to a traditional sea-skimming flight profile. A reduced detection range gives the adversary a shorter reaction time, thereby increasing the missile's survivability [53].

Analyzing Fig. 29, we observe that the first radar detection line decreases by approximately 86 km due to the RF LO RAM coating. The graph indicates that the missile can navigate at high altitudes toward the target and remain undetected. Long-range cruise missiles can use this advantage during a swarming attack. Conversely, a missile in the PEC configuration must operate in a sea-skimming profile to take advantage of the radar horizon, which is about 30 km for a target flying at 2 m and a radar height of 35 m. A closer look at Fig. 30 reveals that nulls can be exploited up to 12 km.

Fig. 31 shows the profiles for the PEC and RAM-coated configurations (sea state 3):

Analyzing Fig. 31, we observe that the first radar detection line decreases by approximately 86 km due to the RF LO RAM coating. However, compared to sea state 1, there are fewer nulls available for high-altitude navigation, limiting swarm operation. As with the sea state 1 configuration, a PEC missile would benefit from low-altitude navigation. A closer look at Fig. 32 reveals that nulls can be exploited up to 12 km.

Fig. 33 shows the profiles for the PEC and RAM-coated configurations (sea state 4):

Analyzing Fig. 33, we observe that the first radar detection line decreases by approximately 90 km due to the RF LO RAM coating. However, compared to sea state 3, there are fewer nulls available for high-altitude navigation. As with the sea state 1 and 3 configurations, a PEC missile would benefit from low-altitude navigation. A closer look at Fig. 34 reveals that nulls can be exploited up to 15 km.

Table 6 summarizes the best operational conditions (RF LO) between PEC/RAM-coated configurations over sea states 1,3, and 4:

The highest observed reduction of 94 s in reaction time for the RAM-coated configuration (sea states 1 and 3) is operationally significant. In real-world scenarios, such delays can critically impair the effectiveness of defensive systems, particularly when engaging low-RCS, fast-moving cruise missiles. As noted by Marzolf [54], the inability to promptly strike time-sensitive targets often results in missed opportunities, as these targets may vanish from the engagement window before a response is possible. Moreover, RF LO inherently interferes with the air defence system OODA (observe-orient-decide-act) loop in its most important phases: observe and orient. This enables the missile to surprise the air defence system of the ship or coastal area and therefore increase the missile survivability [55]. Across sea states 1, 3, and 4, the RAM-enabled trajectories consistently exploit multipath null channels to reduce the detection line and extend the reaction time, thus deconflicting salvo timing and constraining the defender's engagement.

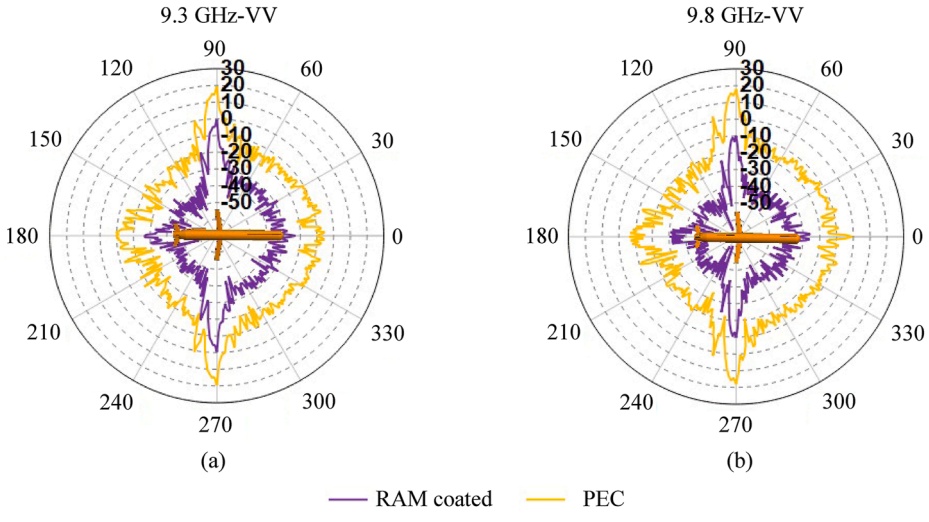

Fig. 26. 9.3/9.8 GHz VV polar graphs: (a) 9.3 GHz VV ($\theta = 90°$); (b) 9.8 GHz VV ($\theta = 90°$).

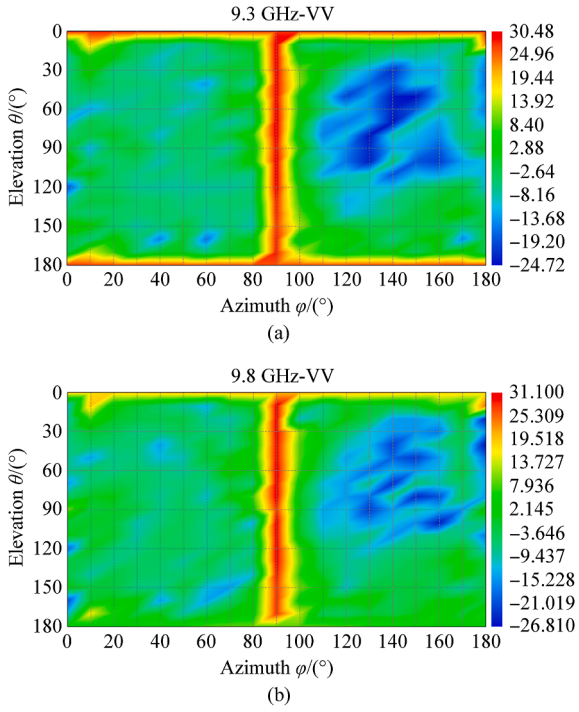

Fig. 27. RCS maps of 9.3/9.8 VV PEC BGM-109 geometry: (a) 9.3 GHz VV PEC RCS map; (b) 9.8 GHz VV PEC RCS map.

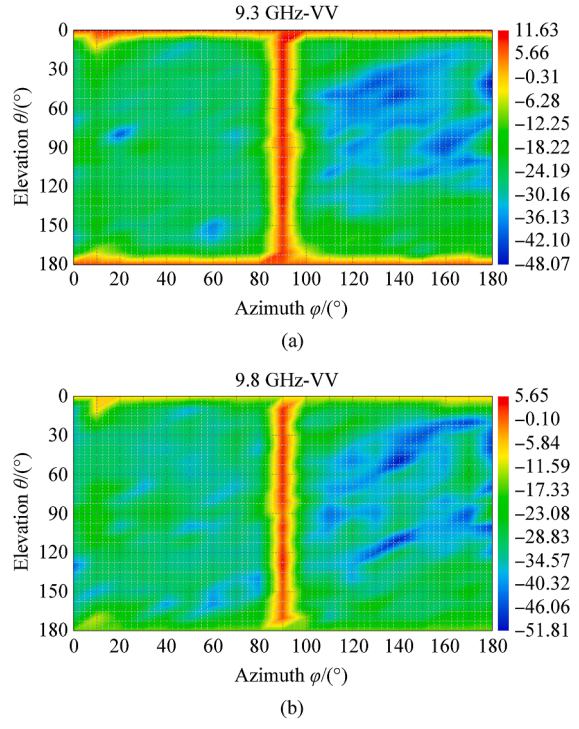

Fig. 28. RCS maps of 9.3/9.8 VV RAM-coated BGM-109 geometry: (a) 9.3 GHz VV RAM-coated RCS map; (b) 9.8 GHz VV RAM-coated RCS map.

5. Conclusions

Multipath is a phenomenon that can significantly impact the radar's detection ability. Optimizing the missile's flight profile within the null channels emerges as a feasible alternative to sea-skimming (one of the ways to evade radar detection). Besides reducing the detection range, the application of RAM coating increases the volume so that the target can fly under the protection of sea multipath. Hence, this feature can be utilized by a swarm of missiles to attack simultaneously the ship or coastal area from different elevations and azimuths. This will cause saturation of the air defence system.

Additionally, the study demonstrates that the integration of MnZn/epoxy RAM with multipath-adaptive flight trajectories yields a measurable delay in radar detection of approximately 94 s. Such a temporal extension is strategically significant, as it alters the defender's engagement timeline by deferring track initiation, constraining operator reaction, and effectively reducing the interception window available to defensive systems.

It is also worth noting that the analysis in this work was intentionally constrained to a simplified flight profile, assuming a direct missile trajectory toward the radar. This approach allowed clearer isolation of the effects of the RAM coating and the sea-surface multipath interaction. Nonetheless, route planning through optimized waypoints combined with small sideslip and incidence angles could enhance stealth performance in realistic operational scenarios. Such maneuvers have the potential to exploit angular scattering variations and maximize RAM effectiveness due to increased angular incidence diversity, possibly yielding RCS reductions beyond those presented in this article.

Table 5
BGM-109 RCS fluctuation summary.

Frequency (Min/Max RCS)	PEC	RAM-coated	RCS reduction
9.3 GHz (Min RCS)	−24.72 dBsm	−48.07 dBsm	23.35 dB
9.3 GHz (Max RCS)	30.48 dBsm	11.63 dBsm	18.85 dB
9.8 GHz (Min RCS)	−26.81 dBsm	−51.81 dBsm	25.00 dB
9.8 GHz (Max RCS)	31.10 dBsm	5.65 dBsm	25.45 dB

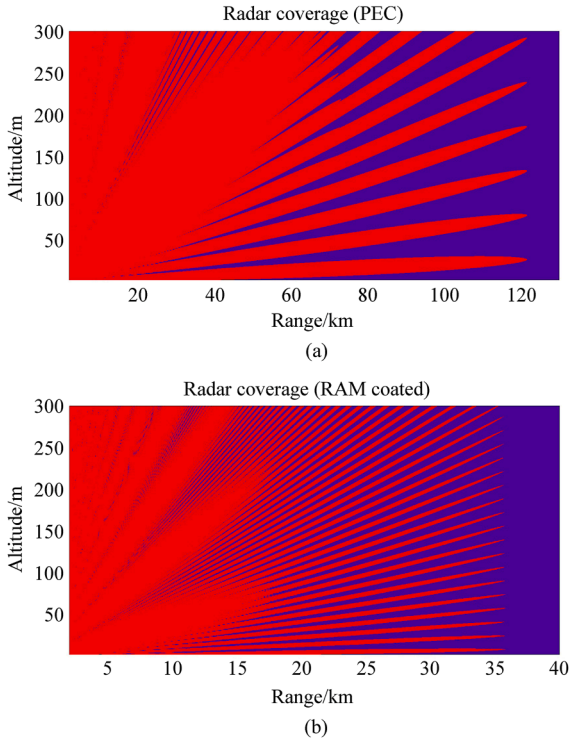

Fig. 29. Radar coverage zones PEC/RAM-coated (head-on profile) sea state 1: (a) Radar coverage zone (PEC) sea state 1; (b) Radar coverage zone (RAM-coated) sea state 1.

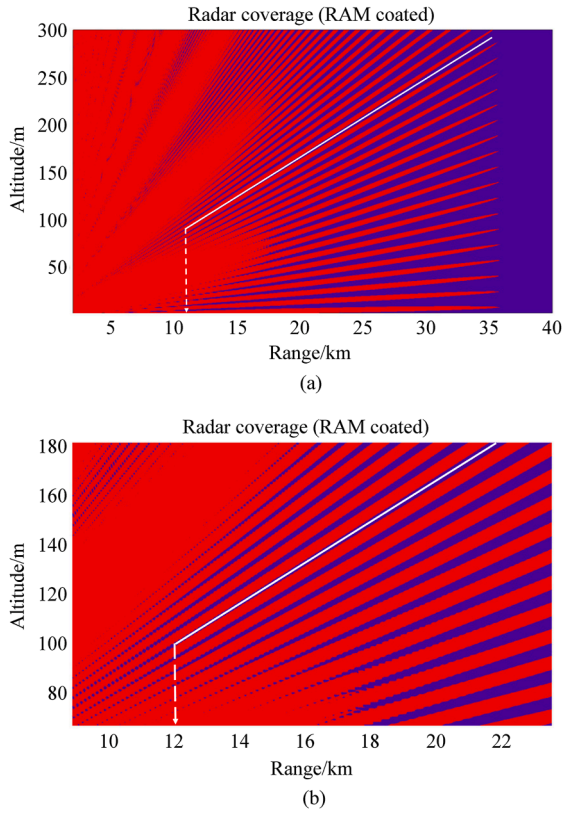

Fig. 30. Radar coverage zones for RAM-coated configuration (head-on profile): (a) Best trajectory for RAM-coated configuration (sea state 1); (b) Zoom-in perspective of the best trajectory (RAM-coated configuration/sea state 1).

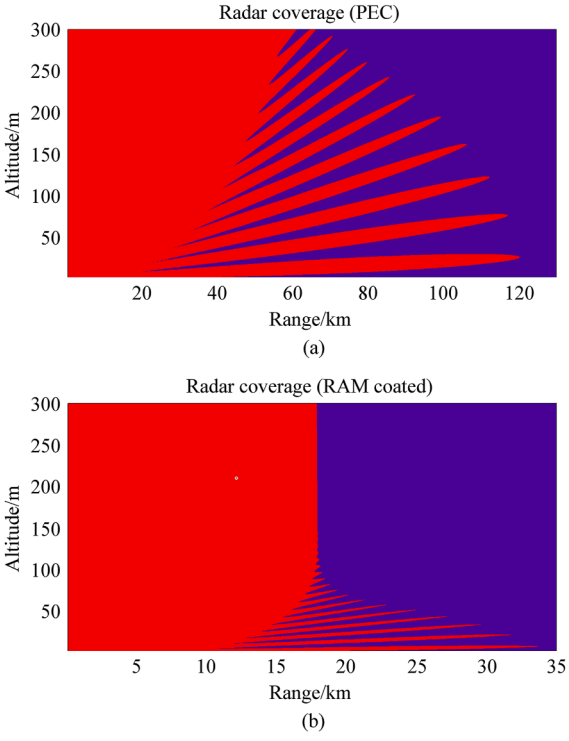

Fig. 31. Radar coverage zones PEC/RAM-coated (head-on profile) sea state 3: (a) Radar coverage zone (PEC) sea state 3; (b) Radar coverage zone (RAM-coated) sea state 3.

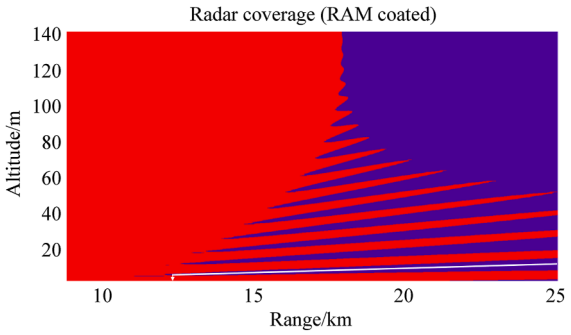

Fig. 32. Zoom-in perspective of the best trajectory (RAM-coated configuration/sea state 3).

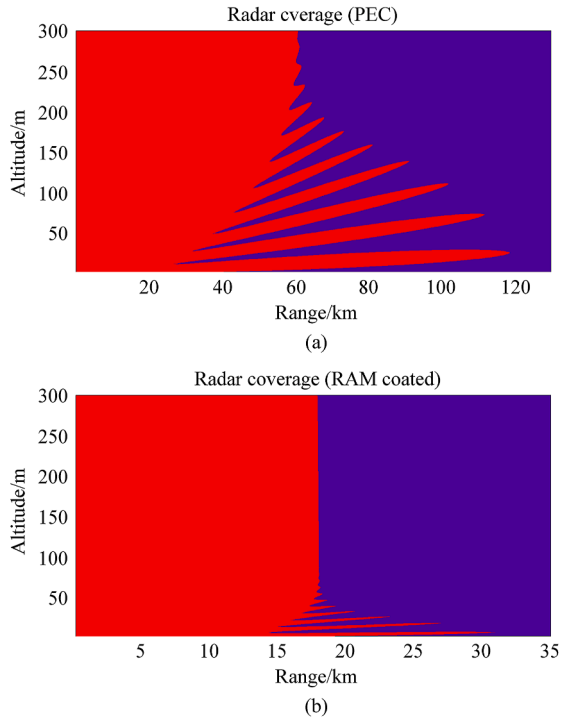

Fig. 33. Radar coverage zones PEC/RAM-coated (head-on profile) sea state 4: (a) Radar coverage zone (PEC) sea state 4; (b) Radar coverage zone (RAM-coated) sea state 4.

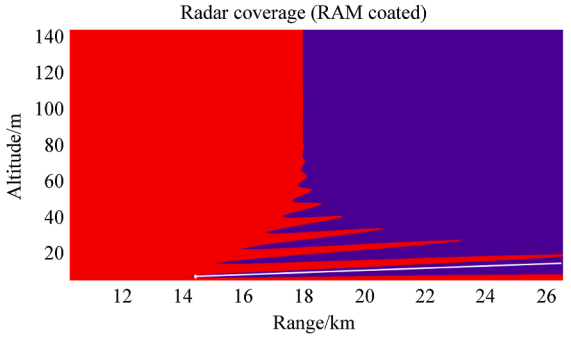

Fig. 34. Zoom-in perspective of the best trajectory (RAM-coated configuration/sea state 4).

Table 6
Operational summary (RF LO profile).

Configuration (Sea state 1)	Detection	Missile altitude	Reaction time
PEC (Sea-skimming)	30 km	2 m	156 s
RAM-coated (High-low)	12 km	290 m–100 m	62 s
Configuration (Sea state 3)	Detection	Missile altitude	Reaction time
PEC (Sea-skimming)	30 km	2 m	156 s
RAM-coated (High-low)	12 km	17 m–7 m	62 s
Configuration (Sea state 4)	Detection	Missile altitude	Reaction time
PEC (Sea-skimming)	30 km	2 m	156 s
RAM-coated (High-low)	15 km	20 m–8 m	78 s

Note: RAM-induced RCS reductions propagate to detection-range deltas via $R \propto \left(F_p^4 \sigma\right)^{1/4}$, yielding the reaction-time extensions ($\Delta t = \Delta R / v_{\text{missile}}$). *Example* (reaction-time, Sea State 1): PEC = 30 km, RAM = 12 km; missile speed = 192 m/s. Reaction-time extension: (30–12) km/192 m/s ≈ 94 s.

As a natural continuation of this research, future work will incorporate advanced algorithmic optimization frameworks to refine RAM composition and geometrical parameters. These strategies will pursue both maximized broadband absorption and RCS reduction and multi-objective constraints related to thermal stability, mechanical robustness, and structural integration in aerospace platforms. Since the present study was conducted at a lower TRL under controlled laboratory conditions with uniform layer thicknesses, subsequent higher-TRL investigations will address accelerated aging, moisture exposure, salt corrosion, and aerothermal durability to validate long-term operational performance. Furthermore, advanced surface-sensitive techniques such as X-ray photoelectron spectroscopy (XPS) will monitor chemical state changes in the ferrite/epoxy interface caused by environmental degradation, and verify ferrite bonding state. Finally, statistical sea clutter modeling to complement the present multipath-based analysis and second-order scattering effects and validation against hybrid solvers such as shooting bouncing ray - physical theory of diffraction (SBR-PTD) remain essential avenues for future steps.

CRediT authorship contribution statement

Renan Richter: Writing – original draft, Visualization, Validation, Software, Project administration, Methodology, Investigation, Formal analysis, Data curation, Conceptualization. **Ioannis Vagias:** Writing – review & editing, Validation, Supervision, Resources, Project administration, Methodology, Investigation, Formal analysis, Conceptualization. **Thalita Sani-Taiariol:** Visualization, Validation, Resources, Investigation, Data curation. **Newton A.S. Gomes:** Writing – review & editing, Supervision, Methodology, Investigation, Formal analysis, Data curation, Conceptualization. **David Bacci:** Writing – review & editing, Supervision, Resources, Methodology, Investigation. **Maurício R. Baldan:** Writing – review & editing, Validation, Supervision, Formal analysis, Data curation.

Declaration of interest statement

The authors declare that they have no known competing financial interests or personal relationships that could have appeared to influence the work reported in this paper.

References

[1] Qing Y, Min D, Zhou Y, Luo F, Zhou W. Graphene nanosheet- and fake carbonyl iron particle-fflled epoxy–silicone composites as thin–thickness and wide-bandwidth microwave absorber. Carbon 2015;86:98–107.
[2] Joseph N, Thomas Sebastian M. Electromagnetic interference shielding nature of pvdf-carbonyl iron composites. Mater Lett 2013;90:64–7.
[3] Feng Y-B, Qiu T, Shen CY, Li XY. Electromagnetic and absorption properties of carbonyl iron/rubber radar absorbing materials. IEEE Transac Magnetics 2006;42:363–8.
[4] Houbi A, Aldashevich ZA, Atassi Y, Bagasharova Telmanovna Z, Saule M, Kubanych K. Microwave absorbing properties of ferrites and their composites: a review. J Magn Magn Mater 2021;529:167839.
[5] Youh MJ, Huang YR, Peng CH, Lin M, Chen TY, Chen CY, Liu YM, Pu NW, Liu BY, Chou CH, Hou KH, Ger MD. Using graphene-based composite materials to boost anti-corrosion and infrared-stealth performance of epoxy coatings. Nanomaterials 2021;11:1603.
[6] Gama AM, Rezende MC. Complex permeability and permittivity variation of radar absorbing materials based on MnZn ferrite in microwave frequencies. Mater Res 2013;16(5):997–1001.
[7] Gama AM, Rezende MC, Dantas CC. Dependence of microwave absorption properties on ferrite volume fraction in MnZn ferrite/rubber radar absorbing materials. J Magn Magn Mater 2011;323(22):2782–5.
[8] de Souza Pinto S, Machado JPB, Gomes NA, Rezende MC. The inffuence of morphology, structure, and weight fraction of magnetic additives on the electromagnetic characteristics of composites. J Magn Magn Mater 2019;484:126–38.
[9] Watts S, Rosenberg L. Challenges in radar sea clutter modelling. IET Radar, Sonar Navig 2022;16(9):1403–14.
[10] Tao M, Zhang Y, Zhang X. Low-angle tracking of shipborne radar. In: 2024 IEEE 6th international conference on power, intelligent computing and systems (ICPICS); 2024. p. 1–4.
[11] Yang Y, Yang B. Overview of radar detection methods for low altitude targets in marine environments. J Syst Eng Electron 2024;35(1):1–13.
[12] Wen B, Wang T, Cheng K. Simulation research on dynamic rcs characteristics of cruise missile. IOP Conf Ser Earth Environ Sci 2019;300(2):022170.
[13] Duc ND, Foroutan K, Varedi-Koulaei SM, Ahmadi H. Nonlinear vibration analysis of laminated composite cylindrical shell under external loading utilizing meta-heuristic optimization algorithms. Iranian J Sci Technol Transac Mech Eng 2023;48:757–77.
[14] Anh VM, Quan TQ, Dat ND, Duc ND. Nonlinear static stability and optimal design of nanocomposite multilayer organic solar cells in thermal environment. Int J Mech Mater Des 2023;19:431–50.
[15] Dat ND, Anh VM, Quan TQ, Pham DT, Duc ND. Nonlinear stability and optimization of thin nanocomposite multilayer organic solar cell using bees algorithm. Thin-Walled Struct 2020;149:106520.
[16] Wang J, Song Y. Thin films and/or coating for electromagnetic interference and stealth. 2021. p. 587–614.
[17] Naito Y, Suetake K. Application of ferrite to electromagnetic wave absorber and its characteristics. IEEE Trans Microw Theor Tech 1971;19(1):65–72.
[18] Si W, Liao Q, Hou W, Chen L, Li X, Zhang Z, Sun M, Song Y, Qin L. Low-frequency broadband absorbing coatings based on MOFs: design, fabrication, microstructure and properties. Coatings 2022;12(6):766.
[19] Jenn DC. Radar cross section. John Wiley & Sons, Ltd; 2024. p. 1–43.
[20] Shu JC, Yang XY, Zhang XR, Huang XY, Cao MS, Li L, Yang HJ, Cao WQ. Tailoring MOF-based materials to tune electromagnetic property for great microwave absorbers and devices. Carbon 2020;162:157–71.
[21] Mahafza BR. Radar systems analysis and design using MATLAB. USA: CRC Press, Inc.; 2000.
[22] Bacci D, Vagias I. A trade-off analysis between lateral/directional stability and radar cross section requirements of an air-to-air combat airframe. Aero Sci Technol 2023;138:108361.
[23] Singh CK, Sinha SD. Effect of terrain bounce jamming on missile guidance in a sea environment. J Battleffeld Technol 2013;16:1.
[24] International telecommunications union radiocommunication sector. Electrical characteristics of the surface of the earth. recommendation. itu-r P.527-6; approved at 27 september, 2021.
[25] Chakrabarti SK. Chapter 3 - ocean environment. In: CHAKRABARTI SK, editor. Handbook of offshore engineering. London: Elsevier; 2005. p. 79–131.
[26] Skolnik MI. Radar handbook. McGraw Hill; 2008.
[27] Nicolson AM, Ross GF. Measurement of the intrinsic properties of materials by time-domain techniques. IEEE Trans Instrum Meas 1970;19(4):377–82.
[28] Pozar D. Microwave engineering. Wiley; 2011.
[29] Jakobus U, Smith G. State of the art of electromagnetic modelling in FEKO. In: 2012 6th European conference on antennas and propagation. (EUCAP), Prague, Czech Republic; 2012. p. 853–4.
[30] Aguilar AG, Jakobus U. Ray-launching geometrical optics in feko: a summary of the last four years of intensive development. In: 2018 international applied computational electromagnetics society symposium - china (ACES); 2018. p. 1–2.
[31] Union IT. Radio Regulations, edition of 2020. International Telecommunication Union; 2020.
[32] Woo A, Wang H, Schuh M, Sanders M. Em programmer's notebook-benchmark radar targets for the validation of computational electromagnetics programs. IEEE Antenn Propag Mag 1993;35(1):84–9.
[33] Shen H, Shi X, Wang Z, Zou P, Hou Z, Xu C, Zhang L, Wu H. Interfacial polarization-dominated dielectric loss in sno2@rgo electromagnetic wave absorbers. Metals 2022;12(12):2154.
[34] Ranjith kumar E, Jayaprakash R, Seehra M, Prakash T, Kumar S. Effect of α-Fe2O3 phase on structural, magnetic and dielectric properties of Mn–Zn ferrite nanoparticles. J Phys Chem Solid 2013;74(7):943–9.

[35] Li Y. Plasmonic optics: Theory and applications, tutorial texts in optical engineering. SPIE Press; 2017.
[36] Petrescu LG, Petrescu MC, Ioniță V, Cazacu E, Constantinescu CD. Magnetic properties of manganese-zinc soft ferrite ceramic for high frequency applications. Materials 2019;12(19):3173.
[37] Low temperature sintered MnZn ferrites for power applications at the frequency of 1 MHz. J Eur Ceram Soc 2021;41(12):5924–30.
[38] Jeyadevan B, Chinnasamy CN, Shinoda K, Tohji K, Oka H. Mn–Zn ferrite with higher magnetization for temperature sensitive magnetic ffuid. J Appl Phys 2003;93(10):8450–2.
[39] Fernández R, Bidegain B, Oyanguren P, Mondragon I. Kinetic studies of the polymerization of an epoxy resin modifed with rhodamine b. Thermochim Acta 2009;493:6–13.
[40] Gonzalez M, Cabanelas J, Baselga J. Applications of FTIR on epoxy resins - identiffcation, monitoring the curing process, phase separation and water uptake. 2012.
[41] Jacobo SE, Bercoff PG, Herme CA, Vives LA. Sr hexaferrite/ni ferrite nanocomposites: magnetic behavior and microwave absorbing properties in the x-band. Mater Chem Phys 2015;157:124–9.
[42] Chen Y, Zhang A, Ding L, Liu Y, Lu H. A three-dimensional absorber hybrid with polar oxygen functional groups of mwnts/graphene with enhanced microwave absorbing properties. Compos B Eng 2017;108:386–92.
[43] Li Y, Huang Y, Qi S, Niu L, Zhang Y, Wu Y. Preparation, magnetic and electromagnetic properties of polyaniline/strontium ferrite/multiwalled carbon nanotubes composite. Appl Surf Sci 2012;258(8):3659–66.
[44] Orfanidis S. Electromagnetic waves and antennas. Sophocles J Orfanidis 2016.
[45] Zhang Y, Liu X, Li J, et al. Hierarchical hollow microspheres assembled from carbon nanosheets integrated with molybdenum carbide nanoparticles for boosting microwave absorption properties. Int J Minerals Metall Mater 2023;30:536–47.
[46] Wang H, Zhao Y, Chen L, et al. Reduced graphene oxide aerogel decorated with mo_2c nanoparticles toward multifunctional properties of hydrophobicity, thermal insulation and microwave absorption. Nano Res 2025;18:94907034.
[47] Wang X, Li Y, Zhang Z, Liu H, et al. Interface engineering in $mose_2$/$nise_2$@c@pc hybrids for enhanced electromagnetic wave absorption. Carbon 2025;239:120327.
[48] Nan K, Zhou Q, Zhang H, et al. Hierarchical porous carbon architectures with multiscale interfaces for broadband microwave absorption and corrosion resistance. Carbon 2025;243:120479.
[49] Xue J, Zhao L, Han Y, et al. Two birds with one stone: multidimensional interfaces and nitrogen doping for ultrathin high-performance microwave absorbers. Chem Eng J 2025;510:161603.
[50] Wang L, Chen Y, Fang J, et al. Schottky barrier engineering at sns2/coni@nc heterointerfaces for broadband electromagnetic absorption. J Mater Sci Technol 2025;232:147–55.
[51] Zhou P, Huang L, Xie J, Liang D, Lu H, Deng L. Prediction of microwave absorption behavior of grading honeycomb composites based on effective permittivity formulas. IEEE Trans Antenn Propag 2015;63(8):3496–501.
[52] Zhao Y, Ren F, He L, Zhang J, Yuan Y, Xi X. Design of graded honeycomb radar absorbing structure with wide-band and wide-angle properties. Int J Microwave Wireless Technol 2018:1–8.
[53] Ball RE. The fundamentals of aircraft combat survivability analysis and design. AIAA education series. 2nd Edition. American Institute of Aeronautics and Astronautics; 2003.
[54] Marzolf GW. Time-critical targeting. Tech. rep., Air Command and Staff College, Air University, Maxwell Air Force Base, Alabama. 2004.
[55] Nicholls DJ. Cruise missiles and modern war: strategic and technological implications. 2012.

Adaptive RF stealth for next-generation long-range cruise missiles through interdisciplinary integration of MnZn ferrite/epoxy RAM and sea-surface multipath null exploitation

Richter, Renan

2026-05

Richter R, Vagias I, Sani-Taiariol T, et al., (2025) Adaptive RF stealth for next-generation long-range cruise missiles through interdisciplinary integration of MnZn ferrite/epoxy RAM and sea-surface multipath null exploitation. Defence Technology, Volume 59, May 2026, pp. 149-165
https://doi.org/10.1016/j.dt.2025.11.010